# Laboratory studies of water ice in space : optical and photochemical properties

Kofman, V.

# Chapter 2

# A multifunctional setup for astronomical ices

**Abstract**

A new multi-functional high vacuum ice setup is described that allows to record the *in situ* and real-time spectra of vacuum UV (VUV) irradiated non-volatile molecules embedded in a low temperature (10 K) amorphous solid water environment. Three complementary diagnostic tools – UV-visible (UV-vis), Fourier Transform Infrared (FTIR) spectroscopy, and Temperature Programmed Desorption Quadrupole Mass Spectrometry (TPD-QMS) – can be used to simultaneously study the physical and chemical behavior of the organic molecules in the ice upon VUV irradiation. The setup is equipped with a temperature controlled sublimation oven that enables the controlled, homogeneous deposition of solid species such as amino acids, nucleobases and polycyclic aromatic hydrocarbons (PAHs) in ice mixtures prepared from precursor gases and/or liquids. The resulting ice is photoprocessed with a microwave discharge hydrogen lamp, generating VUV radiation with a spectral energy distribution relevant for the interstellar medium.

The characteristics, performance, and future potential of the system are discussed by describing three different applications. First, a new method is introduced that uses broadband interference transmission fringes recorded during ice deposition, to determine the wavelength dependent refractive index, $n_\lambda$, of amorphous solid water. This approach is also applicable to other solids, pure and mixed. Second, the UV-vis and FTIR spectroscopy of a VUV irradiated triphenylene:water ice mixture is discussed, monitoring the ionization

Kofman, V., Witlox, M. J. A., Bouwman, J., ten Kate, I. L. and Linnartz, H. 2018 "A multifunctional setup to record FTIR and UV-vis spectra of organic molecules and their photoproducts in astronomical ices" In: *Rev. Sci. Instrum.*, 89, 053111

efficiency of PAHs in interstellar ice environments. The final example investigates the stability of solid glycine upon VUV irradiation by monitoring the formation of dissociation products in real-time.

## 2.1 Introduction

Ice is an important reservoir of the molecular inventory in the colder and denser regions of the interstellar medium (ISM). When particle densities increase and temperatures are sufficiently low, atoms and molecules accrete and/or react on the surface of carbonaceous and silicate dust grains. This results in the formation of tens of monolayers comprising of different ice species. Space-based infrared observations with the ISO and Spitzer space telescopes have identified some 12-14 different ice constituents (Gibb et al., 2004; Öberg et al., 2011; Boogert et al., 2015), including $H_2O$, CO, $CO_2$, $CH_3OH$, $CH_4$, and $NH_3$. The assignment of the astronomical data was possible with the help of infrared spectra recorded for pure and mixed ices under fully controlled laboratory conditions, *i.e.*, in full dependency of the ice temperature and mixing ratios. Many more species are expected to be present in the solid phase. It is generally accepted that chemical processes in the bulk and on the surface of interstellar ices are essential in facilitating the formation of both rather simple species such as $H_2O$ (Ioppolo et al., 2008; Miyauchi et al., 2008) and $CH_3OH$ (Fuchs et al., 2009) and more complex species including small sugars and alcohol sugars, like glycolaldehyde and glycerol (Ioppolo et al., 2011; van Dishoeck et al., 2013; Bergin and Tafalla, 2007; Garrod et al., 2008; Herbst and van Dishoeck, 2009; Fedoseev et al., 2017; Linnartz et al., 2015). Laboratory experiments, indeed, confirmed that molecular complexity in an ice environment can be enhanced through (radiation-induced) radical recombinations (Bernstein et al., 2002; Öberg et al., 2009a), atom addition and abstraction reactions (Chuang et al., 2016; Chuang et al., 2017; Linnartz et al., 2015) or upon thermally induced processes during warm-up (Muñoz-Caro et al., 2002; Butscher et al., 2017; Nuevo et al., 2010; de Marcellus et al., 2015a).

Alternatively, larger species such as polycyclic aromatic hydrocarbons (PAHs), typically formed in the ejecta of dying stars, may also directly freeze out onto icy grains. Their characteristic vibrational gas phase features are observed as infrared emissions along many different lines of sight, but these vanish in regions where these species are expected to freeze out. (Allamandola et al., 1989; Tielens, 2013) It is therefore very likely that PAHs, like other volatiles, will accrete onto cold dust grains, resulting in a solid state PAH

reservoir in space. So far, unambiguous solid state identifications of these larger species, both complex organic molecules and PAHs, is limited by lacking solid-state spectra or because broad and overlapping features do not allow to make unambiguous assignments. In fact, the limited number of solid state identifications contrasts strongly with the more than 200 gas phase identifications of molecules in the ISM of which many are thought to have a solid state origin.

Since the 1970s astrophysical ice mixtures have been studied in the laboratory, mostly using Fourier Transform Infrared (FTIR) spectroscopy. Over decades, a special focus has been on the impact of energetic (VUV) photons on mixed ices originating from the interstellar radiation field and it was shown that many organics can be found in the residues left over after irradiation, *e.g.* (Hagen et al., 1979; Muñoz-Caro et al., 2002; Bernstein et al., 2002; Meinert et al., 2016). To this day, infrared spectroscopy remains the go-to technique in laboratory ice astrochemistry, recording vibrational modes of the solid components. This enables one to assign typical absorption bands relatively easily, but also comes with the problem that similar vibrational modes in different molecules exhibit about the same spectroscopic behavior; peak positions are not unique and solid state features are typically broad, which complicates unambiguous identifications. Terminal and secondary functional groups are likely to have unique spectral signatures, but larger species are difficult to discern. This complicates the spectroscopic detection of molecules containing more than three carbon atoms. Another issue is that astronomical ice matrices, particularly water, strongly absorb in the IR. Therefore, in many laboratory IR ice studies, mostly pure or rather high concentrations of specific precursors have been used; this fails to represent realistic astronomical mixing ratios and will influence the chemical processes taking place. Optical, *i.e.*, electronic ice spectroscopy offers a useful alternative.

Some 15 years ago the first systematic studies of UV-vis ice absorption were reported (Gudipati and Allamandola, 2003; Gudipati and Allamandola, 2004; Gudipati, M. S. and Allamandola, 2006). These come with a number of advantages over infrared studies. Water, the astronomically most abundant ice constituent, is transparent in this wavelength range and this allows to use much lower concentrations of embedded species, particularly as transition strengths in the UV-vis can be orders of magnitudes stronger, further enabling the study of very dilute (and astronomically more relevant) mixtures. Another advantage of UV-vis spectroscopy is its higher time resolution: IR spectrometers are typically slow compared to their optical counterparts, which makes the monitoring of ongoing chemical processes in real-time difficult.

So far, most reported UV-vis ice experiments have been focusing on PAHs embedded in amorphous water environments, see *e.g.* (Gudipati and Allamandola, 2003; Gudipati and Allamandola, 2004; Bouwman et al., 2010; Guennoun et al., 2011; Lignell and Gudipati, 2015). Many PAHs and their cations have large electronic oscillator strengths and absorb in the UV, visible or near IR, which facilitates such experiments, even for dilute mixtures. Studies have been reported previously of UV-vis spectra of PAHs and ionized PAHs embedded in water and ammonia environments (Cuylle et al., 2012). It was found that water ice decreases the ionization potential of the embedded PAHs, favoring the formation of cations (Gudipati and Allamandola, 2004), and that ammonia ice tends to enhance the formation of PAH anions (Cuylle et al., 2012). With higher water temperatures (40 K vs. 10-20 K) the formation of hydrogenated and hydroxygenated PAHs was seen at the expense formation of the cation (Guennoun et al., 2011; Cook et al., 2015). It was also found that the concentration of the solute influences the ionization efficiency (Cuylle et al., 2014a). An unfortunate disadvantage of UV-vis ice studies is that the assignment of electronic bands is harder to link to specific molecules than in the IR, and theoretical data are needed for assignments. Moreover, astronomical identifications of optical transitions of ices in space are currently still lacking.

The use of either IR or UV-vis spectroscopy to study interstellar ices clearly has its pros and cons. Combining both methods, therefore, offers an opportunity to benefit from the strengths of both methods and to link information obtained in one wavelength domain to findings in the other. Here we describe a new setup capable of recording both UV-vis and FTIR of VUV photoprocessed ice spectra *in situ* and quasi in real-time, monitoring ongoing dynamics in the ice. We demonstrate the use of UV-vis spectroscopy to track reaction products formed on a seconds time-scale, and infrared spectroscopy to study the photostability of precursor species and photoinduced end-products. A complementary quadrupole mass spectrometer offers a further tool to identify (newly formed) ice constituents. Below we describe the experimental details and procedures and illustrate the potential of this setup on three selected examples: i) the determination of the refractive index, $n(\lambda)$, for amorphous solid water (ASW) at 10K between 250 and 750 nm, ii) the VUV photochemistry of triphenylene ($C_{18}H_{12}$) in ASW at 10 K and iii) the formation of HCN and $\cdot$CN from glycine upon VUV irradiation in an argon matrix at 10 K as a tool to monitor the photostability of frozen amino acids.

## 2.2 System Description

Figure 2.1 shows a 3D schematic drawing, illustrating the concept of the new setup. The system comprises a central high vacuum chamber onto which the cold head of a closed cycle helium refrigerator is mounted. Ices grown on a UV-vis and IR transparent window mounted on the tip of the cold finger can be irradiated with the VUV light from a microwave hydrogen discharge lamp and ice constituents, deposited, consumed and formed are monitored using a broadband UV-vis and FTIR spectrometer as well as a quadrupole mass spectrometer that monitors ice constituents during thermal desorption.

### 2.2.1 Main Chamber

The central part of the setup consists of an ISO 160 6-way crosspiece, in which four additional CF 35 connections have been welded between the ISO ports, all directed towards the center of the cross piece. The vacuum chamber is mounted onto an optical table (250x125 cm), that carries the two spectrometers and all necessary optical components.

One of the ISO ports supports a turbomolecular pump (Leybold 350 iX turbovac ISO 100, 290 l/sec for $N_2$), backed up by a two-stage 8 $m^3$/hr rotary pump, realizing a base pressure of the order of $10^{-8}$ mbar. To prevent oil from entering the system a high-temperature cracking trap is placed on top of the prepump, which also reduces the load with potentially toxic species by thermally cracking these.

On the top flange of the vacuum chamber the cold head of a closed cycle helium cryostat is mounted (DE202NE, Advanced Research Systems, Inc.) via a turnable feedthrough. At the tip of the cold finger, a $BaF_2$ window is mounted that is transparent from 140 nm to 16.7 $\mu$m. The sample temperature is controlled through resistive heating using a LakeShore 330 temperature controller. Temperatures between 10 and 325 K are accessible and measured using a factory calibrated Al-Cr thermocouple with an absolute precision better than 2 K.

Ices are grown onto the cold sample through direct deposition at a normal angle, using a 1/4 inch Swagelok tube mounted 15 mm from the surface. A precision dosing valve (Pfeiffer EVN 116), equipped with a digital display for the setting, is used to control the flow of gas phase or liquid precursor species.

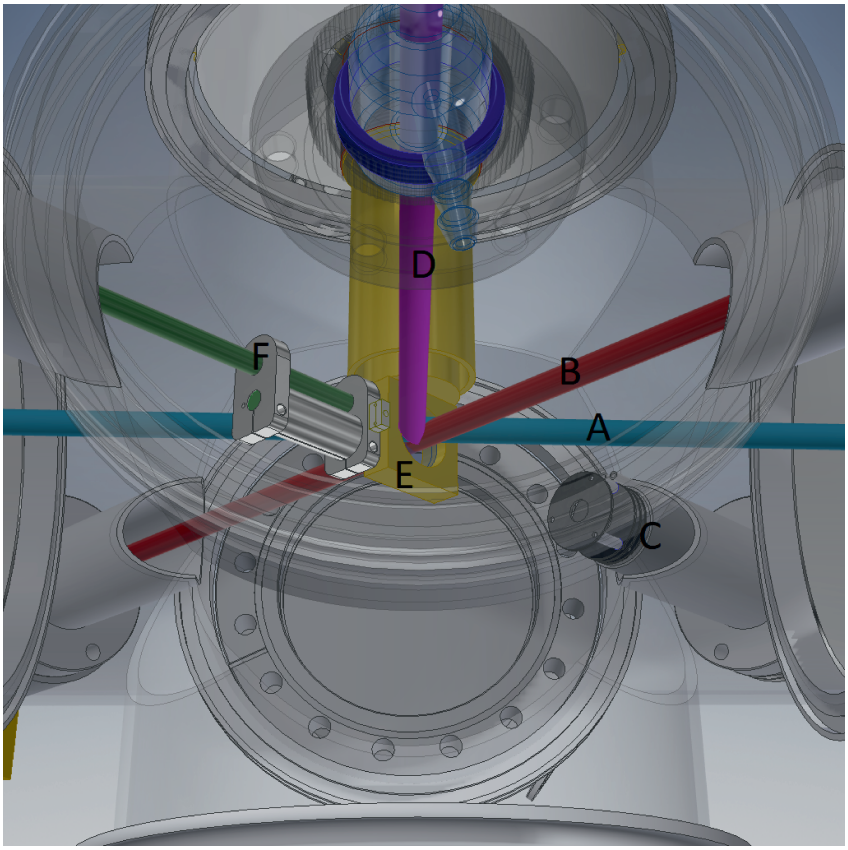


FIGURE 2.1: 3D drawing of the interior of the vacuum system. The characters indicate the following: A. UV-vis path; B. Fourier Transform Infrared path; C. Quadrupole Mass Spectrometer; D. Vacuum ultraviolet light source; E. Cryostat with $BaF_2$ window; F. gas inlet and sublimation oven.

A custom designed and built oven, fully mounted inside the vacuum chamber, serves as a source to sublimate non-volatile molecules that can be co-deposited simultaneously with the ice. The oven is temperature controlled, and has a temperature precision better than 0.2 °C, which is needed to guarantee a homogeneous deposition rate. The maximum temperature is roughly 150 °C, which is more than sufficient to sublimate the amino acids and the small to medium PAHs targeted here. A 1/4 inch Swagelok tube, closed off at one end, is used as precursor reservoir. The reservoir slides into the oven and is removable, thus eliminating the need to detach the entire oven system from the vacuum chamber to add or replace the amino acids/PAHs. The orifice of the oven is positioned roughly 15 mm from the sample surface. In this configuration dilution ratios can be realized as low as PAH:$H_2O$ = 1:10,000.

A microwave hydrogen discharge lamp (MHDL) is used as a VUV light source. These lamps have been used for decades to simulate interstellar radiation fields (Warneck, 1962), peaking around Ly-$\alpha$ (121 nm) and 160 nm ($H_2$ emission). In a series of recent papers MDHL characteristics and their dependence on different settings have been discussed in detail (Muñoz-Caro and Schutte, 2003; Chen et al., 2014; Ligterink et al., 2015; Es-sebbar et al., 2015). In our setup, a 150 W, 2450 MHz Opthos microwave generator is used to run a plasma at 0.5 mbar $H_2$ (grade 5.0) gas. The effective power of the generator is 100 Watt. The resulting VUV flux amounts to 1-2 $\times$ $10^{15}$ photons/cm$^2$ s at the sample surface, a value that is derived using oxygen/ozone actinometry (Cottin et al., 2003; Fulvio et al., 2014). The MHDL is connected to the main chamber via a $MgF_2$ window (25 mm diameter and 4 mm thickness). A tube is placed inside the chamber, which guides the light directly onto the sample. Stable and clean $H_2$ flows in the MDHL are guaranteed using a small rotary pump that is equipped with an oil trap.

### 2.2.2 Spectrometers

The ice mixtures are studied using two different spectrometers, covering the wavelength domain associated with electronic and vibrational ice mode transitions.
UV-vis light (200-1100 nm) is generated using a deep UV xenon arc light source (150W LOT- QuantumDesign). The white light beam is spatially filtered by two subsequent pinholes, and transmitted through a $MgF_2$ (25 mm diameter and 4 mm thickness) window onto the ice substrate (positioned at 45° with respect to the UV-vis beam). Light then exits the vacuum chamber through another $MgF_2$ window and is focussed on the slit of an UV-vis spectrometer (Andor

303i Shamrock), equipped with a CCD (Andor iDus DV420_OE) responsive to photons between 200 and 1100 nm. The available resolution depends on the used grating, where the spectral range coverage can be extended at the expense of a lower resolution. The maximum resolution accessible is 0.05 nm, with a spectral coverage of roughly 50 nm. In our ice experiments, a larger spectral range is favored over resolution. For the example experiments described later, spectra are recorded from 200 to 760 nm with a resolution of 0.56 nm. To guarantee that the absolute wavelength calibration is well within any uncertainties for the used resolution, emission from the overhead fluorescence light, HeNe light and emission from the xenon arc lamp are used to correct for grating offsets.

During a regular experiment, UV-vis spectra are taken every 4.3 seconds, and such an averaged spectrum is the result of 120 individual spectra. The system allows for much higher time resolution, but for the experiments described below this is not necessary. Data taken after deposition are plotted as difference spectra with respect to the initially deposited sample.

Two CF 35 ports are used to transmit infrared light (2.5-16.7 $\mu$m / 4000-600 $cm^{-1}$) through the ice. An optical system consisting of gold-coated plano and concave mirrors are used to guide and focus the light from the external beam port of a Biorad FTS 3000 spectrometer onto the sample. A 90° focusing mirror collects the IR light on a liquid $N_2$ cooled mercury-cadmium-tellurium (MCT) detector. The typical resolution used amounts to 2 $cm^{-1}$. Higher resolution is possible, but this increases the measurement time per spectrum significantly and is not required for the solid state experiments such as those reported here. ZnSe windows are used as vacuum seals. The IR beam path is purged with dry air and $CO_2$ free air. A background spectrum is recorded before the deposition. In this way, the IR spectra reflect the entire sample processing (unlike the UV-vis spectra). Typically 200 measurements are averaged, resulting in a time resolution of roughly 5 minutes.

The setup has been constructed in such a way that both spectrometers can be used simultaneously (Figure 2.1). Two different orientations are used. In position 1 the sample faces the deposition oven and is rotated 90 ° with respect to the infrared beam path. This orientation is used for deposition and allows to perform UV-vis spectroscopy and VUV photoprocessing at the same time, both at an angle of incidence of 45°. In position 2 (shown in Figure 2.1), the sample faces the infrared beam, thus allowing transmission infrared spectroscopy at a normal angle, as well as the UV-vis beam at a 45° angle of incidence (this time passing the sample back to front). VUV processing is done at 45°. Additional

TABLE 2.1: Sample characteristics of the two triphenylene:water experiments.

| Experiment | $d$ [nm] | $C_{18}H_{12}$:$H_2O$ | Column density [molecules $cm^{-2}$] UV-vis | 1497 $cm^{-1}$ | 1437 $cm^{-1}$ | 1253 $cm^{-1}$ |
|---|---|---|---|---|---|---|
| 1 | 247 | 1:906 | $7.6 \times 10^{14}$ | $1.5 \times 10^{15}$ | $2.7 \times 10^{15}$ | $2.0 \times 10^{15}$ |
| 2 | 858 | 1:3642 | $7.0 \times 10^{14}$ | $1.5 \times 10^{15}$ | $2.3 \times 10^{15}$ | $2.1 \times 10^{15}$ |

deposition from the oven in this orientation is hindered, as the substrate faces the side of the copper sample holder.

Besides the two spectrometers, the setup is equipped with a quadrupole mass spectrometer (Pfeiffer Prisma Plus QMG 220) that is placed at one of the remaining CF 35 ports. This complementary tool allows us to link UV-vis and/or IR signals to species desorbing at specific temperatures, typically through their characteristic fragmentation patterns upon 70 eV electron impact ionization which are available from the NIST database (Stein, 2018). Mass spectra covering up to 300 *m/z* are taken in bar graph mode, reporting the entire range of *m/z* values at a resolution of 1 amu.

### 2.2.3 Preparation and characterization of the sample

Triphenylene:water samples are prepared by heating the oven to the sublimation temperature of triphenylene (65 °C) and two different ice thicknesses are realized by dosing water for 50 minutes at pressures of $0.5 \times 10^{-8}$ mbar and $1.7 \times 10^{-8}$ mbar above the base pressure (see Table 1). Commercial triphenylene powder (roughly 5 mg per fill, 98+ % purity) is used without further purification. For the water matrix, ultra-pure milli-Q generated water is degassed in several freeze-pump-thaw cycles before use.

Matrix isolation experiments on glycine in argon are performed. Glycine is sublimated at an oven temperature set of 105 °C, and is deposited with argon (99.999 % purity) at a sample temperature of 10 K. Prior to the sample deposition the window is placed parallel with respect to the oven sample position, preventing triphenylene or glycine to deposit onto the sample before the desired temperature is established. Deposition is started by opening the dosing valve and rotating the sample so that it faces the sublimation oven and deposition line, *i.e.* we rotate the sample from position 2 to position 1. During deposition, UV-vis spectra are continuously taken. After completing the deposition, the sample is rotated and FTIR spectra are recorded. This

allows us to study the ice growth during deposition with UV-vis, and after rotation the VUV induced end products with both UV-vis and FTIR.

## 2.3 Results and Discussion

### 2.3.1 A new approach to measure ice thicknesses

The sample thickness is an important parameter, as it has to be known to determine the concentration of the solutes under investigation. When ice is photoprocessed by VUV light, the thickness also determines the photon penetration depth. Ice thicknesses are generally determined by recording the interference fringes that arise from a laser beam reflecting at the sample surface and at the top of the ice layer. The path length difference between the two light beams results in constructive and destructive interference signals, which change with increasing ice thickness (Baratta and Palumbo, 1998; Dohnálek et al., 2003; Bossa et al., 2014). The intensity of the reflected light is measured with a photodiode. This results in a sinusoidal signal, where the period between the maxima ($m$) is related to the thickness $d$ according to equation 2.1.

$$d = \frac{m \times \lambda}{2 \times n_\lambda \times \cos\theta} \tag{2.1}$$

Here, $\lambda$ is the wavelength, $n_\lambda$ the refractive index of the ice and $\theta$ the angle of incidence (45° in our setup).

In our system, using UV-vis spectroscopy, an alternative approach is possible that in addition offers the possibility to derive the full wavelength dependent refraction index of an (amorphous) ice. The applied principle is rather similar, but instead of looking for interference fringes by one external laser, fringes superimposed on the UV-vis transmission signal are used. This eliminates the need for an additional laser and photodiode and instead, the same broadband Xe arc-light and spectrometer can be used that are also needed for the spectroscopic investigation. An example of interference fringes seen at a number of selected wavelengths is shown in Figure 2.2. For the full investigation, fringes are recorded for hundreds of wavelengths at the same time. Clearly, the fringing is more pronounced for shorter wavelengths, but visible over the full range. The figure also shows, that over a set time interval for shorter wavelengths the number of fringes, $m$, is larger than for longer wavelengths, in agreement with equation 2.1. This now allows, in principle,

to derive ice thicknesses for any wavelength, but as the refractive index is wavelength dependent, $n_\lambda$ needs to be known first. For crystalline ice, these numbers are available from Warren and Brandt (2008) and show a variation with wavelength that gets more pronounced towards the UV. It should be noted these values are for relatively high ice temperatures (in the astronomical context) and only measured at low resolution. For amorphous water ice only a very limited number of $n_\lambda$ values is known and for practical reasons generally restricted to the HeNe wavelength, 632.8 nm. Dohnálek et al. (2003) report a value of 1.285 for compact ASW with a density of 0.94 g/cm$^3$ at this wavelength. These values are not strongly temperature dependent but depend mostly on porosity (Dohnálek et al., 2003; Bouilloud et al., 2015). Using this refractive index and assuming a density of 0.94 g/cm$^3$ for our ice, we calculate thicknesses of 247 and 858 nm for the thin and thick ice experiments as listed in Table 1. This now provides all information needed to derive $n_\lambda$. In a Python routine the number of fringes is determined for all recorded wavelengths, *i.e.*, quasi-continuous and for many more than the selected points shown in Figure 2.2. Three separate experiments have been performed. The derived $n_\lambda$ curves are colored gray in Figure 2.3. A fit through all data points, averaging the values from the individual measurements, results in a curve that is indicated in black and that clearly deviates from the values for crystalline ice, shown with the blue curve in Figure 2.2 (Warren and Brandt, 2008). Typical deviations of 5-10 % exist when comparing the three experimental curves. This is acceptable, given the fact that these data are fully lacking in the literature. The strength of this method is that it is relatively easy to determine $n_\lambda$ for a large wavelength domain - it takes less than a day to derive one curve - and that these numbers can be determined with decent accuracy. As the method is generally applicable, this approach can be easily used to derive wavelength dependent refractive indexes for other ices, pure and mixed. In fact, the method also will work fine for crystalline ices, which will allow a further fine-tuning. Work to use this method to provide $n_\lambda$ graphs of astronomically relevant ices is currently in preparation.

### 2.3.2 Triphenylene:water ice mixtures; column densities and VUV photochemistry

In order to determine the concentration of a solute, two parameters are needed, its abundance - which can be determined from the absorbance - and the ice thickness, as derived above. In the UV-vis, the abundance or column density can be quantified by integrating the area under an electronic transition ($\tau_{el}$) and

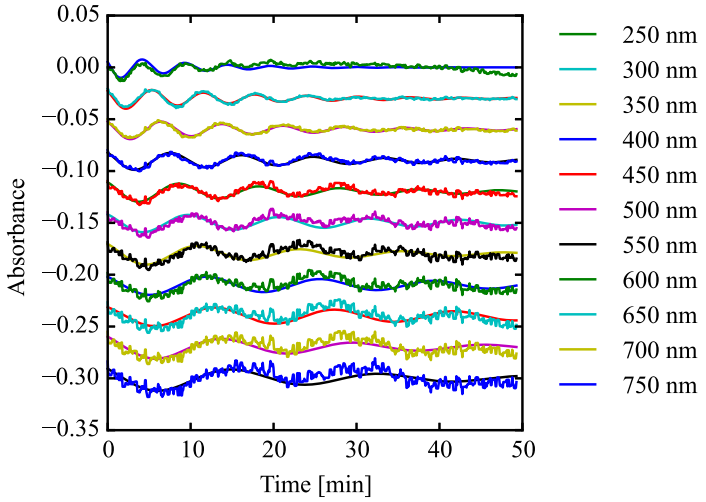


FIGURE 2.2: Interference signal superimposed on the UV-vis signal as a function of time. A sinus multiplied with an exponential decay is fit to the signal and overplotted. The legend indicates the wavelength at which the signal is taken.

dividing this by the oscillator strength $f$ and a factor as reported in Kjaergaard et al. (2000):

$$N_{el} = \frac{\int_{v1}^{v2} \tau_{el} dv}{8.85 \times 10^{-13} \times f} \tag{2.2}$$

In the experimental literature absorption is often reported as the extinction coefficient, $\epsilon_{max}$. To convert this to $f$, one uses (Malkin, 1992):

$$f = \frac{4.39 \times 10^{-9}}{n_\lambda} \int \epsilon dv \tag{2.3}$$

For triphenylene, a value of $\epsilon_{max}$ = 174,000 has been reported in (Malkin, 1992).

Infrared transitions can be used in a similar way to quantify the column density:

$$N_{vr} = 2.303 \times \frac{\int_{v1}^{v2} \tau_{vr} dv}{S} \tag{2.4}$$

where the factor 2.303 converts the values from natural to base 10 logarithm, and $\int_{v1}^{v2} \tau_{vr} dv$ is the integrated infrared band strength of the transition and $S$ is the transition strength in cm$^{-1}$ per molecule.

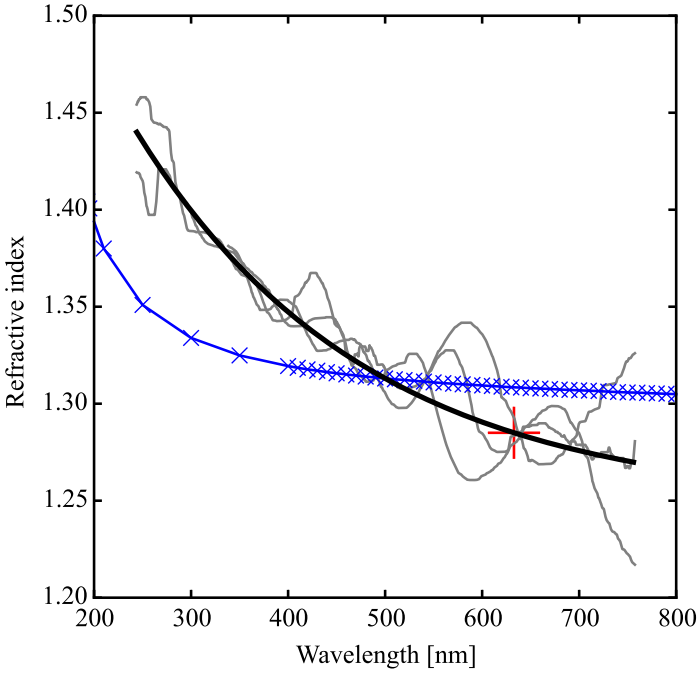


FIGURE 2.3: Refractive indices, $n_\lambda$ as determined by the method described above for amorphous solid water at 10 K, shown in black. The new values are based on three experiments shown in gray. The $n_\lambda$ values of crystalline water ice are shown in blue (Warren and Brandt, 2008); the value reported in Dohnálek et al. (2003), which is used as a calibration point, is plotted as a red cross.

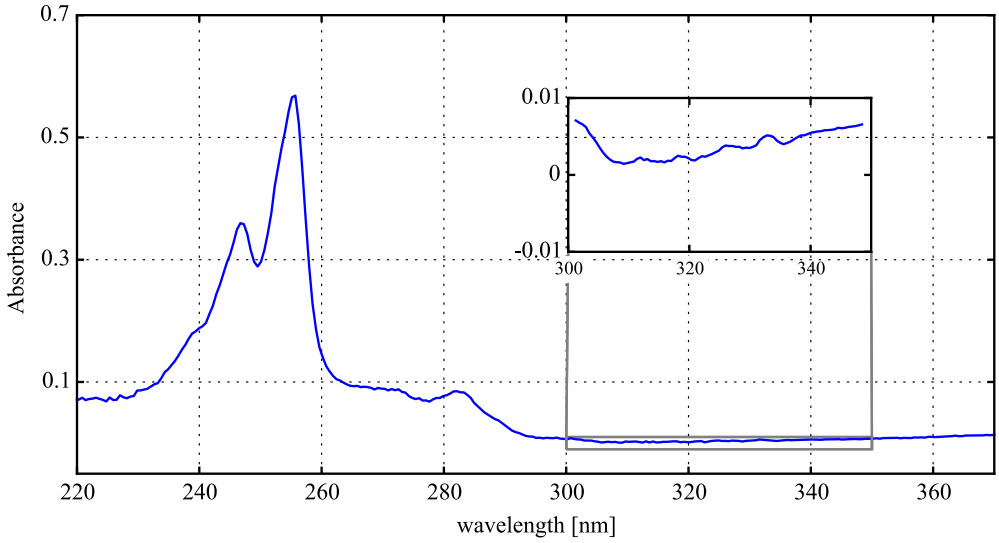


FIGURE 2.4: UV-vis spectrum of triphenylene in water. $S_3 \leftarrow S_0$ is seen at 255 nm, $S_2 \leftarrow S_0$ at 285 and the inset shows the weak $S_1 \leftarrow S_0$ transitions. All of the transitions display strong vibronic components. This spectrum is taken from experiment 2.

Figure 2.4 shows the UV-vis spectrum of triphenylene in water as seen in the thin and thick ice experiments. The spectra are similar in both cases, except for a slight broadening of the features in the first case. For this reason, only the thick ice case is shown. The spectral signatures of neutral triphenylene are observed at 255 nm for $S_3 \leftarrow S_0$ and at 284 nm for $S_2 \leftarrow S_0$. A weak series of transitions is found around 330 nm $S_1 \leftarrow S_0$, shown in more detail in the inset. These assignments are made based on existing matrix isolation studies (Kokkin et al., 2007; Kofman et al., 2017). The reproducibility with which non-volatile species can be sublimated and deposited onto the substrate is illustrated by showing the maximum triphenylene absorption signal around 255 nm as a function of time for the two ice thicknesses studied here. In the left panel of Figure 2.5 these signals are shown as a function of time. Deposition starts at 0 and is in both experiments continued for about 50 minutes. The high reproducibility is clear from the nearly identical growth curves. After the deposition, the sample is rotated, and a new reference spectrum is taken, which resets the signal to 0. After a short interval, the VUV irradiation is started which results in the consumption of precursor material. Upon VUV irradiation, part of the neutral precursor is transferred into cationic triphenylene, the spectrum of the cation is presented in Figure 2.6. This has been observed for

other PAHs in the past (Gudipati and Allamandola, 2003; Gudipati, M. S. and Allamandola, 2006) and is illustrated in the right part of Figure 2.5. Clear triphenylene cation signals are found at 402 nm, and broader features at lower wavelengths. Cation production works best for dilutions of the order of less than 1:1000 (PAH:$H_2O$) (Cuylle et al., 2014b). Here, the maximum ion column density is seen after roughly 15 minutes of irradiation. The formation yield of the cation is then roughly 30 %, taking a transition strength of the cation of $f = 0.11$ (Keszthelyi et al., 2000). Maximum yield is realized during the first few minutes of irradiation and is around 45 %.

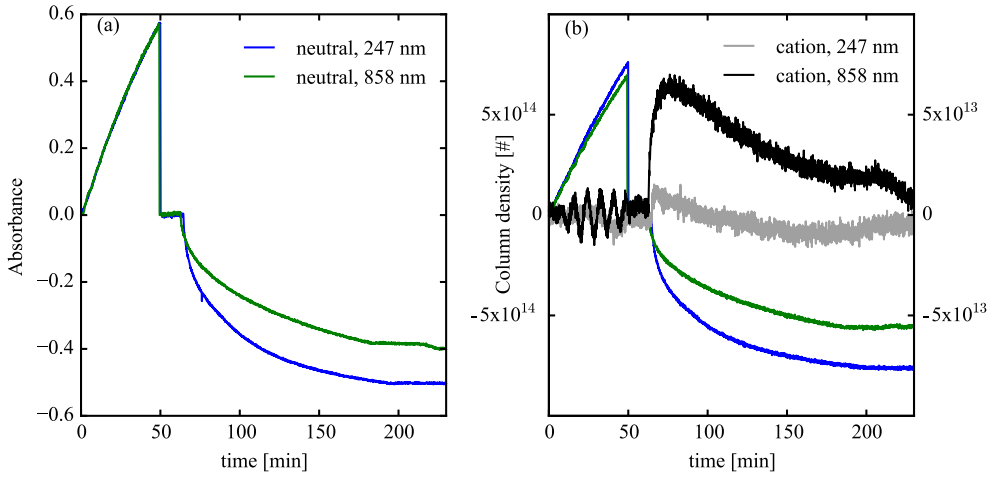


FIGURE 2.5: (a) The time-dependent absorbance of the ($S_3 \leftarrow S_0$) transition of triphenylene recorded at a wavelength of 255 nm for the ices of two thicknesses (blue 247 nm and green 858 nm). (b) Column densities for the experiment shown in (a) including also the VUV induced ion signals. The cation column densities are plotted on the right y-axis. Negative features correspond with decreasing column density, and positive features reflect cation formation.

For the thick ice, this process is less efficient than for the thin ice, which can be understood as in the latter case the VUV light reaches a larger fraction of the ice. In the right panel of Figure 2.5 the integrated absorbance is shown, both for the precursor material (that largely follows the curves in the left panel), and for the reaction product, the triphenylene cation. As the ionization efficiency is higher at lower concentrations, the cation formation is more effective in the thicker ice. Thus, although less neutral precursor material is consumed, a larger column density of cations are produced in the thicker ice with the lower triphenylene concentration.

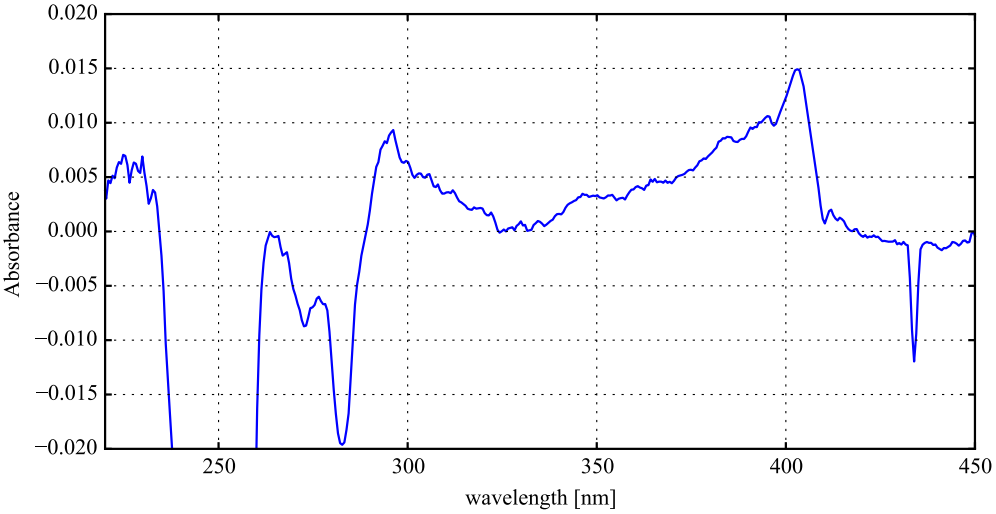


FIGURE 2.6: UV-vis spectra of VUV irradiated triphenylene water mixture. Upon VUV irradiation neutral $C_{18}H_{12}$ is destroyed, resulting in negative absorbance. Positive features are absorptions related to the cation. The strongest of these is seen at 402 nm, having several broad features towards shorter wavelengths.

Infrared spectra of triphenylene in water ice are shown in Figure 2.7. The spectra are from the experiment where the concentration of triphenylene in water is roughly 1:900 (experiment 1). The spectrum illustrates that water signals largely dominate the spectrum, but the zoom-in shows that sufficient sensitivity is realized to also record the PAH bands. The theoretical band positions and band strengths are plotted as well, and this illustrates that the position and relative intensities reproduce well (Langhoff, 1996; Boersma et al., 2014; Bauschlicher et al., 2018). The following bands are visible in the diluted water matrix: 1437 $cm^{-1}$ most likely corresponding to two modes at 1440 $cm^{-1}$ having a combined band strength of $7.8 \times 10^{-18}$ $cm^{-1}$ per molecule; similarly two transitions at 1253 $cm^{-1}$ ($1.1 \times 10^{-18}$ $cm^{-1}$ per molecule) and two at 1497 $cm^{-1}$ ($4.2 \times 10^{-18} cm^{-1}$ per molecule).

Using the available literature values for triphenylene, we derive for the two experiments listed in Table 1, column densities of 7.6 and $7.0 \times 10^{14}$ molecules $cm^{-2}$ by integrating the UV-vis transition between 222 and 268 nm. The equivalent exercise in the IR (at 1500, 1440 and 1253 $cm^{-2}$) results in column densities that are approximately two to three times larger. It is very likely that this mismatch is due to an underestimate of the used band strengths as calculated by DFT methods. This is in line with conclusions by

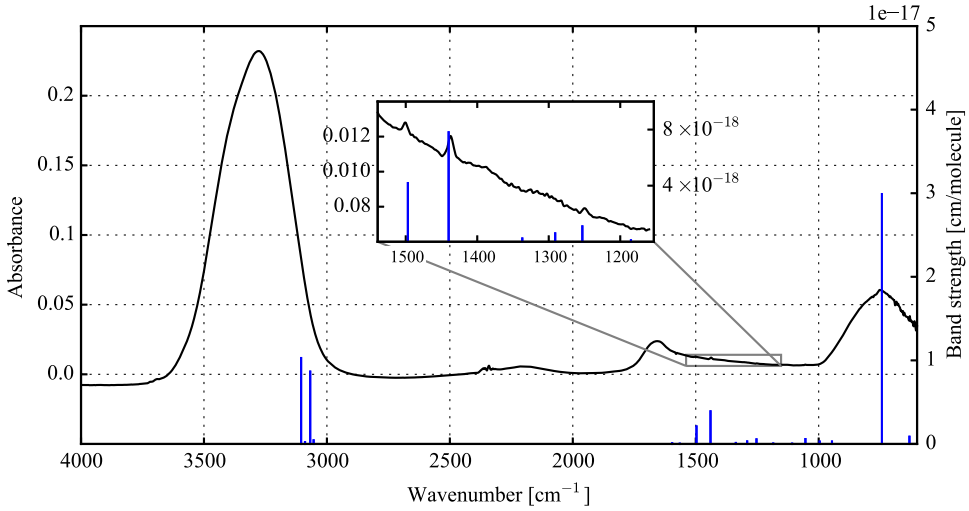


FIGURE 2.7: Infrared spectrum of neutral triphenylene in water. Blue bars are the transitions of neutral triphenylene as predicted by Langhoff (1996), corresponding to the y-axis on the right side. The inset shows a part of the fingerprint region.

Hardegree-Ullman et al. (2014) who find theoretical pyrene band strengths 50 % larger than experimentally derived by Bouwman et al. (2011).

Whereas the neutral precursor signals, though weak, are clearly visible, no IR features can be assigned to modes of the triphenylene cation. Based on the computed band strengths, we can estimate whether we should be able to. Assuming a maximum column density of roughly $6 \times 10^{13}$ molecules cm$^{-2}$, cation signals should be visible when the band strengths from Langhoff (1996) are taken, but as discussed before such band strengths may have been overestimated. Clearly here UV-vis spectroscopy offers a powerful alternative.

### 2.3.3 Photochemistry of glycine

The recent detection of glycine, the smallest amino acid, on comet 67P (Altwegg et al., 2016) has further strengthened the idea that complex organic molecules are formed in outer space on solid surfaces. Clearly, the formed glycine has been able to withstand the intense radiation in space. Understanding the photochemistry of this amino acid under VUV radiation is key in explaining its presence on comets and possibly other celestial objects. An experimental

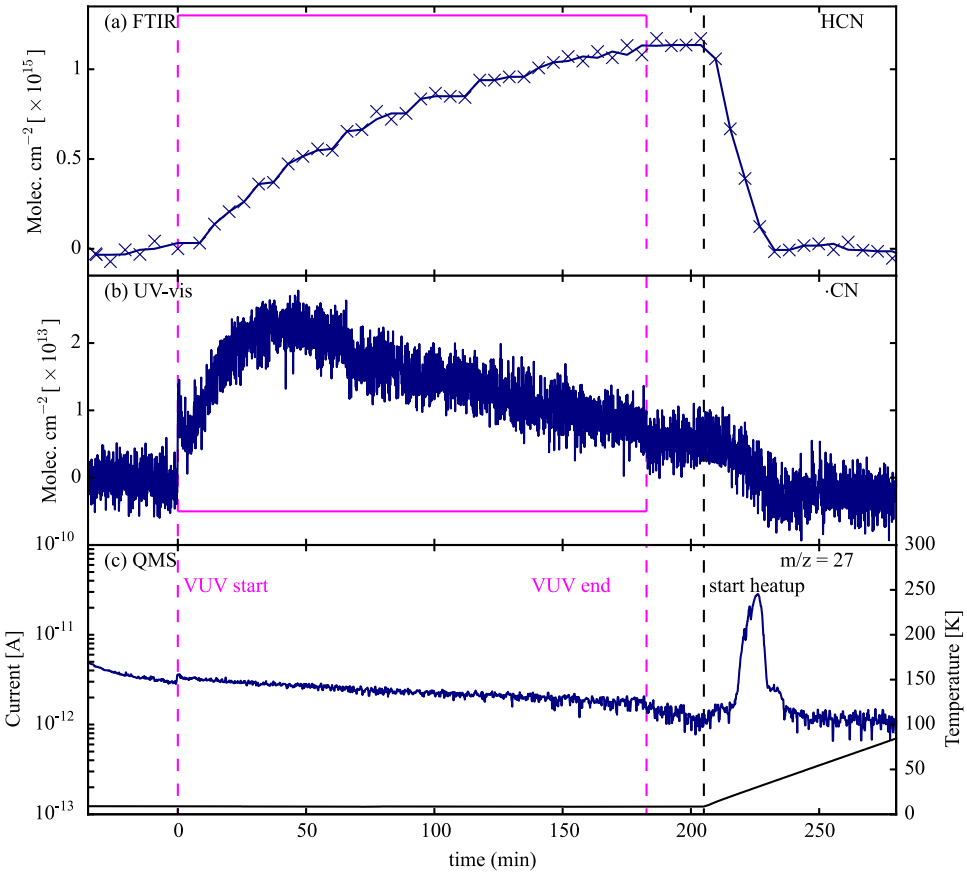


FIGURE 2.8: Production of HCN as a function of time (*i.e.* fluence). VUV irradiation is indicated with the dashed vertical magenta lines ($t = 0$ min and $t = 180$ min); the black dashed lines indicate the start of the ice heating ($t = 210$ min).
(a) Column density of HCN derived from the transitions at 2091 cm$^{-2}$. The reported band strength is $5.1 \times 10^{-18}$ cm$^{-1}$ per molecule. (Bernstein et al., 1997) (b) Column density of ·CN, derived from the transition at 380 nm. Note the integrated column density is much smaller than shown in (a). (c) $m/z$ = 27 (HCN) signal measured with the QMS, which is the main signal seen upon electron impact of HCN.

way of investigating the photostability of this amino acid, or other biologically relevant species, is by monitoring the time-dependent formation of fragments resulting from the photoinduced dissociation. We have studied this by VUV irradiation of glycine embedded in an argon matrix. Although not present in space, argon ice provides a chemically inert environment to study this process without the need to take into account other reactions due to a water matrix. Argon also provides a suitable host to trap produced radical species. Indeed upon VUV irradiation, and consistent with what has been reported in the literature (*e.g.* Ehrenfreund et al. (2001)) HCN is formed from the fragmentation of frozen glycine. This can be understood by looking at the photodegradation mechanism:

$$\mathrm{NH_2CH_2COOH} \xrightarrow{h\nu} \mathrm{CH_3NH_2} + \mathrm{CO_2}$$
$$\mathrm{CH_3NH_2} \xrightarrow{h\nu} 2\,\mathrm{H_2} + \mathrm{HCN}$$

In Figure 2.8(a) the integrated infrared absorbance of HCN is shown, which absorbs at 2091 $\mathrm{cm}^{-1}$. The assumed band strength is $5.1 \times 10^{-18}$ $\mathrm{cm}^{-1}$ (Bernstein et al., 1997). Also shown in this figure are start and end times of the VUV processing, indicated by the magenta vertical lines. HCN is produced relatively slowly (the half-life time of glycine is in the order of a few minutes under these conditions), which is in agreement with the hypothesis that it is formed as a secondary product from the photodegradation of the formed methylamine. In addition to the infrared detection of HCN, we see the formation of the $\cdot$CN radical in the UV-vis, which absorbs between 376 and 384 nm. Figure 2.8(b) shows the integrated band of $\cdot$CN in the UV-vis ($f = 0.00320$ (Danylewych and Nicholls, 1978)). $\cdot$CN is formed at the start of the VUV processing. A maximum column density of roughly $2 \times 10^{13}$ molecules per $\mathrm{cm}^2$ is found after around 40 minutes, and subsequently, it is destroyed. In the period between the end of the irradiation and start of the heat-up, $\cdot$CN is stable.

The third panel (c) shows the results from parallel QMS experiments monitoring $m/z = 27$, the dominant HCN $m/z$ signal upon electron impact ionization. A heating ramp is started roughly 30 minutes after the end of the VUV processing. The temperature of the sample is also indicated in Figure 2.8 (c), placed on the secondary y-axis (right side). The black line reports the temperature. A maximum of $m/z = 27$ is seen coinciding with the disappearance of the respective species in (a) and (b). Panel (c) also shows the temperature axis of the TPD.

As the measurements are performed simultaneously, the abundances of the products can be directly linked. The formation of ·CN from glycine has not been reported in the literature. From the formation kinetics, it appears to be formed earlier in the photodegradation than HCN, enabling the possibility that HCN is formed from the hydrogenation of ·CN. This would imply that the photochemical degradation of glycine results in different products depending on the environment, as the ·CN radical is highly reactive and could form different end products. An extensive study, also looking at Gly in water, is in preparation.

## 2.4 Astrophysical potential

Observations with the ISO and Spitzer Space Telescopes have shown that icy dust grains comprise of different chemical components, layered and intimately mixed, amorphous and crystalline, porous and compact. So far, some twelve different ice constituents have been identified in the interstellar medium. With the upcoming launch of the James Webb Space Telescope, a new visible-infrared observatory (2019), it will become possible to investigate interstellar ices at spectral and spatial resolutions and sensitivities, orders of magnitude better than possible before. This will offer a view on the 'Icy Universe' in unprecedented detail, also along lines of sight hard to observe up to now, *e.g.*, towards the distant, crowded Galactic Center and the Magellanic Clouds. As icy dust grains are the formation place of complex organic molecules (COMs), which have been identified with the Atacama Large Millimeter Array in the gas phase, this also offers a tool to bridge the grain-gas-gap. Moreover, with the completion of the Extremely Large Telescope in the UV-NIR in 2024, also the recording of optical ice spectra towards embedded objects will become possible. The full scientific impact of these observations, however, only will be realized when astronomical observations and astrochemical models can make use of precise laboratory ice data, ranging from spectroscopic data to wavelength-dependent refractive indices and recorded for known compositions, mixing ratios, temperature, porosity levels, and other parameters.

The setup described here offers this opportunity. It is expected that the number of solid-state identifications will quickly increase. This information and combined with gas phase detections of larger species in space will allow us to learn more about the solid-state processes at play. Also here the present setup can contribute, by visualizing the chemical processes taking place.

In this chapter, the potential to study the behavior of PAHs and glycine upon VUV irradiation in cryogenic matrices has been illustrated. In the recent past, much focus has been put onto so-called 'GRAND PAHs', large polycyclic aromatic hydrocarbons with typically more than 40-50 C-atoms. Their presence in space has been explicitly linked to the observation of the aromatic infrared bands (Allamandola et al., 1989), and several studies on their photofragmentation behavior have been recently reported. Compact and strongly bound smaller PAHs may be relevant as well; triphenylene ($C_{18}H_{12}$) belongs to this category as it is fully benzenoid. Other COMs are observed in the gas phase as well, and as only solid-state pathways offer the efficiencies to explain their formation, it is clear that experiments are needed to characterize both their spectroscopic and dynamical features, like for the glycine discussed here.

## 2.5 Acknowledgments

Financial support through the NWO program PEPSci (Planetary and ExoPlanetary Science) and a NWO VICI grant is acknowledged. The authors thank Niels Ligterink, Ko-Ju Chuang, Sergio Ioppolo and Sergio Pilling for input and discussions regarding the design of the setup. Raymond Koehler is thanked for designing and building the oven controller. This research has made use of NASA's Astrophysics Data System.